https://doi.org/10.5194/egusphere-2026-1845
Preprint. Discussion started: 16 April 2026
© Author(s) 2026. CC BY 4.0 License.

# Mohr–Coulomb yield curves for viscous-plastic sea ice models: flow rules and failure angles

Damien Ringeisen[1,3,4,5], L. Bruno Tremblay[1], Jean-François Lemieux[2], and Martin Losch[3]

[1]Department of Atmospheric and Oceanic Sciences, McGill University, Montréal, QC, Canada
[2]Recherche en Prévision Numérique Environnementale, Environnement et Changement Climatique Canada (ECCC), 2121 route Transcanadienne, Dorval, Qc, Canada.
[3]Alfred-Wegener-Institut, Helmholtz-Zentrum für Polar- und Meeresforschung, Bremerhaven, Germany
[4]MARUM – Center for Marine Environmental Sciences, Bremen, Germany
[5]Canadian Centre for Climate Modelling and Analysis, Environment and Climate Change Canada (ECCC), Victoria, British Columbia, Canada.

**Correspondence:** Damien Ringeisen (damien.ringeisen@ec.gc.ca)

**Abstract.** Viscous-plastic sea ice models typically overestimate the intersection angle between conjugate pairs of Linear Kinematic Features (LKFs) in uni-axial compression tests. These models employ an elliptical yield curve with a normal flow rule. Mohr–Coulomb yield curve formulations can use different plastic potentials (elliptical, teardrop, parabolic lens) implying different flow rule orientations along the limbs of the Mohr–Coulomb yield envelope. The flow rule affects not only the LKFs intersection angle, but also the numerical convergence of the model and the approach to transitions between viscous and plastic states. Some of the proposed Mohr–Coulomb yield curves results in failure angles in the observations 15-30 degree range, which is generally smaller than the ones obtained with the elliptical yield curve with a normal flow rule. The simulated failure angles are best described by Arthur's theory, where both shape of the yield curve and plastic potential influence the orientation of the failure lines. These new Mohr–Coulomb formulations, in particular the Mohr–Coulomb yield curve with elliptical plastic potential with wide ellipse ($e < 2$) or the Mohr–Coulomb yield curve with the teardrop plastic potential, provide interesting alternatives to the elliptical yield curve for the modeling of LKFs in high-resolution sea ice models, at the cost of a less efficient numerical convergence.

## 1 Introduction

The Mohr–Coulomb yield criterion – a simple linear relationship between normal and shear stress at failure – is commonly used to describe the response of some granular materials such as soil and rocks to applied load (Verruijt, 2018; Handin, 1969; Kaus, 2010; Lemiale et al., 2008), and to a lesser extent for sea ice (Ip et al., 1991; Hibler and Schulson, 2000; Dansereau et al., 2016; Tremblay and Mysak, 1997). Specifically, the Mohr–Coulomb criterion defines the critical shear stress (second invariant, $\sigma_{\mathrm{II}}$) as a linear function of the compressive stress (first invariant, $\sigma_{\mathrm{I}}$):

$$\sigma_{\mathrm{II}} = -\mu\sigma_{\mathrm{I}} + c, \qquad (1)$$

© Author(s) 2026. CC BY 4.0 License.

where $\mu = \sin(\phi) > 0$, is the slope coefficient, $\phi$ is the internal angles of friction, $c$ is the cohesion (or shear strength when no normal stress is applied). This mathematical relation derives from a parametric equation of a circle (called the Mohr's circle of stress) that represents all possible shear and normal stress combination on any plane orientation at a point (Mohr, 1882). In sea ice models, we express the cohesion $c$ as function of $\mu$ and the tension $T = k_t P$ (König Beatty and Holland, 2010), expressed as the tensile factor $k_t$ and the compressive strength $P$. The Mohr–Coulomb relationship becomes

$$\sigma_{\mathrm{II}} = -\mu\sigma_{\mathrm{I}} + \mu k_t P. \tag{2}$$

In a plastic model, a flow rule is necessary to close the system of equations. This equation links the critical stresses (or yield curve) and resulting (post-failure) strain rates (or deformation) and defines the relative amount of shear and divergence for a given stress state on the yield curve. Under the assumption of isotropy and no rotation, the principal axes of strain rate and stress coincide. In this case, the flow rule is perpendicular to the yield curve and is called an associative or a normal flow rule. Alternatively, if the directions of the principal stress and the principal strain rate do not coincide, the flow rule is non-normal and the maximum/minimum (normal or shear) deformation and stress do not occur on the same planes (see also, Ringeisen et al., 2021).

Both in situ observations and laboratory experiments show a linear relationship between the shear and normal stresses at failure in accord with Mohr–Coulomb theory (Schulson et al., 2006; Weiss et al., 2007). Moreover, the distribution of the intersection angles between conjugate pairs of LKFs derived from high-resolution satellite images in the Arctic suggests that (1) the elliptical yield curve overestimates the angles between LKFs (Hutter et al., 2022) and (2) that a Mohr–Coulomb yield curve is physically better justified than an elliptical yield curve (Ringeisen et al., 2023a).

The orientation ($\theta$) of LKFs or shear bands relative to the principal stresses has been studied extensively in granular materials. Three main concepts are inferred from experiments with granular media: (1) the Coulomb angle $\theta_C$ defined from the internal angle of friction $\phi$ (i.e., the ratio of normal to shear stress along the LKFs Coulomb, 1773), (2) the Roscoe angle $\theta_R$ defined from the dilatancy angle $\delta$ (i.e., the ratio of divergent to shear deformation Roscoe, 1970), and (3) the Arthur's angle $\theta_A$ that includes the effects of both the internal angle of friction and dilatancy:

$$\theta_{\mathrm{C}} = \frac{\pi}{4} - \frac{\phi}{2}, \tag{3}$$

$$\theta_{\mathrm{R}} = \frac{\pi}{4} - \frac{\delta}{2}. \tag{4}$$

$$\theta_{\mathrm{A}} = \frac{\pi}{4} - \frac{\phi+\delta}{4} = \frac{1}{2}\left(\theta_{\mathrm{R}} + \theta_{\mathrm{C}}\right), \tag{5}$$

Based on experimental data, $\theta_C$ describes small grain size behaviour and $\theta_R$ large grain sizes (Vermeer, 1990). When $\phi = \delta$, all three angles coincide ($\theta_C = \theta_R = \theta_A$). The Coulomb, Roscoe, and Arthur theories are useful paradigms to describe sea ice deformation using a plastic rheology, where the failure angle is dictated by the stress state at failure, the post-failure deformation or a combination of the two. The failure angles of the Mohr–Coulomb yield criterion in sea ice have been studied before like here but in the framework of elastic-brittle rheological framework (Plante and Tremblay, 2021; Dansereau et al., 2019) but not in the VP rheological framework. Other numerical frameworks might be interesting for studying the relationship between

https://doi.org/10.5194/egusphere-2026-1845
Preprint. Discussion started: 16 April 2026
© Author(s) 2026. CC BY 4.0 License.

failure angles and dilatancy, especially Discrete Element Models (DEM) (e.g., Herman, 2016; Damsgaard et al., 2018; Åström et al., 2023).

The Mohr–Coulomb yield curve was introduced for pan-Arctic simulations in the context of a viscous-plastic sea ice model, but it did not lead to improvement in the sea ice drift compared to buoy data (Ip et al., 1991). Subsequently, the model was reformulated within a cavitating fluid framework, where shear strength replaced bulk viscosity, yielding a shear-only flow rule, and the internal ice pressure was solved using a Poisson equation (Flato and Hibler, 1992). A different model used a double sliding flow rule (based on Balendran and Nemat-Nasser, 1993) to introduce a dilatancy angle and create open water along shear lines (Tremblay and Mysak, 1997). Other formulations of Mohr–Coulomb yield curves (Hibler and Schulson, 2000; Hutchings et al., 2005; Wang and Wang, 2009) have not been extensively used in realistic pan-Arctic simulations. Further, the original formulation (Ip et al., 1991) does not converge numerically with a realistic angle of internal friction $\sin(\phi) \simeq 0.7$ (Lemieux and Dupont, 2020). As observations still suggest that sea ice behaves as a granular material governed by a Mohr–Coulomb yield criterion, so that is remains interesting to explore Mohr–Coulomb formulations in spite of the limited success in sea-ice models. A successful Mohr–Coulomb rheological formulation would feature a good numerical convergence (comparable to the elliptical yield curve) and LKFs intersection angles in the same range as observations.

To this end, we report results from uni-axial loading experiments with four formulations (two published and two new) of the Mohr–Coulomb criterion in the VP rheological model, namely, the original formulation of Ip et al. (1991), a truncated Mohr–Coulomb yield curve with an elliptical yield curve (Hibler and Schulson, 2000), and two new formulations with a teardrop and parabolic lens plastic potentials, inspired by the results of (Ringeisen et al., 2023b). We show that the details of the transition from the viscous to the plastic regimes have a large influence on the numerical convergence and that Mohr–Coulomb yield curve formulations with an appropriate plastic potential result in failure angles within the observed ranges.

The manuscript is organized as follows. The different Mohr–Coulomb formulations are described in Section 2. The uni-axial compression experimental setup is described in Sect. 3. The result of these experiments are presented in Sect. 4, and the discussions and conclusions are given in Sect. 5 and 6.

## 2 Mohr–Coulomb viscous-plastic rheologies

### 2.1 Momentum equation and VP rheological framework

We model sea ice as a viscous-plastic material. The ice velocity $\boldsymbol{u}$ is calculated from the momentum equation:

$$\rho h \frac{\partial \boldsymbol{u}}{\partial t} = \nabla \cdot \boldsymbol{\sigma} - \rho h f \boldsymbol{k} \times \boldsymbol{u} + \boldsymbol{\tau}_a + \boldsymbol{\tau}_o - \rho h \nabla \phi_s, \tag{6}$$

where $\boldsymbol{\sigma}$ is the vertically integrated internal ice stress tensor defined by the sea ice VP constitutive equations, $\rho$ is the ice density, $h$ is the averaged sea ice thickness, $f$ is the Coriolis parameter, $\boldsymbol{k}$ is the vertical unit vector, $\boldsymbol{\tau}_a$ is the surface air stress, $\boldsymbol{\tau}_o$ is the ocean stress, and $\nabla \phi_s$ is the acceleration from the gradient of sea surface height.

We use the general form of the constitutive equations written in terms of the stress and strain rate (Reiner-Rivlin equation)

$$\sigma_{ij} = 2\eta \dot{\epsilon}_{ij} + (\zeta - \eta)\, \dot{\epsilon}_{kk} \delta_{ij} - p \delta_{ij}, \tag{7}$$

https://doi.org/10.5194/egusphere-2026-1845
Preprint. Discussion started: 16 April 2026
© Author(s) 2026. CC BY 4.0 License.

where $p$ is the rheology-dependent stress coefficient that depend on the ice strength $P$, and $\zeta$, and $\eta$ are the bulk and shear viscosities. We keep $p$ as function of the ice compressive strength $P$ and tensile factor $k_t$ to generalize the equations, as it is necessary to derive constitutive equations (Ringeisen et al., 2023b). For instance, for the elliptical rheology as defined by Hibler (1979), $p = \frac{P}{2}$, while for the elliptical yield curve with isotropic tensile strength as define by König Beatty and Holland (2010), $p = \frac{P(1-k_t)}{2}$, and for the teardrop yield curve with normal flow rule, it is $p = \frac{P(2-k_t)}{3}$ (Ringeisen et al., 2023b).

Equation (7) can also be written in terms of the stress invariants as:

$$\sigma_{\mathrm{I}} = \zeta \dot{\epsilon}_{\mathrm{I}} - p, \tag{8}$$

$$\sigma_{\mathrm{II}} = \eta \dot{\epsilon}_{\mathrm{II}}, \tag{9}$$

where

$$\sigma_{\mathrm{I}} = \frac{1}{2}(\sigma_{11} + \sigma_{22}), \qquad \sigma_{\mathrm{II}} = \frac{1}{2}\sqrt{(\sigma_{11} - \sigma_{22})^2 + 4\sigma_{12}^2}, \tag{10}$$

$$\dot{\epsilon}_{\mathrm{I}} = \dot{\epsilon}_{kk} = \dot{\epsilon}_{11} + \dot{\epsilon}_{22}, \qquad \dot{\epsilon}_{\mathrm{II}} = \sqrt{(\dot{\epsilon}_{11} - \dot{\epsilon}_{22})^2 + 4\dot{\epsilon}_{12}^2}. \tag{11}$$

The local maximum compressive strength $P$ in isotropic convergence is defined as a function of the ice thickness $h$ and concentration $A$ as

$$P = P^{\star} h e^{-C^{\star}(1-A)}, \tag{12}$$

where $P^{\star}$ is the compressive strength of 1 m thick ice in isotropic compression (typically $P^{\star} = 27.5\,\mathrm{N\,m^{-1}}$) and $C^{\star}$ a parameter relating ice strength to ice concentration, typically, $C^{\star} = 20$.

Each Mohr–Coulomb rheological model presented below differs only by their definition of the $\zeta$, $\eta$ and $p$ terms. Four different non-normal flow rule are considered: one with only pure shear flow rule (flow rule always pointing vertically upward) (MC-PS, Ip et al., 1991) and three others with an elliptical (MC-E), teardrop (MC-TD), and parabolic lens (MC-PL) plastic potentials.

### 2.2 The Mohr–Coulomb rheology with pure shear flow rule (MC-PS)

The MC-PS constitutive relations can be derived using four different methods, yielding the exact same forms. For the sake of brevity, we present these derivations in Appendix A. The resulting constitutive equations are

$$\zeta_{\mathrm{MC-PS}} = \frac{P(1+k_t)}{2|\dot{\epsilon}_{\mathrm{I}}|}, \tag{13}$$

$$\eta_{\mathrm{MC-PS}} = \frac{\mu\left(\frac{P(1+k_t)}{2} - \zeta\dot{\epsilon}_{\mathrm{I}}\right)}{\dot{\epsilon}_{\mathrm{II}}} = \mu\frac{P(1+k_t)}{2}\frac{\left(1 - \frac{\dot{\epsilon}_{\mathrm{I}}}{|\dot{\epsilon}_{\mathrm{I}}|}\right)}{\dot{\epsilon}_{\mathrm{II}}}, \tag{14}$$

$$p_{\mathrm{MC-PS}} = \frac{1-k_t}{2}P, \tag{15}$$

and $\sigma_{ij}$ as defined by Eq. (7).

https://doi.org/10.5194/egusphere-2026-1845
Preprint. Discussion started: 16 April 2026
© Author(s) 2026. CC BY 4.0 License.

In Ip et al. (1991), for small deformation, the viscosities were capped at a maximum value $\zeta_{\max}$, $\eta_{\max}$ or a minimum was set on $\dot{\epsilon}_{\mathrm{I}}$ and $\dot{\epsilon}_{\mathrm{II}}$, a small number $\epsilon_{\min}$. Here we use a smoother transition between plastic and viscous states by replacing $|\dot{\epsilon}_{\mathrm{I}}|$ by $\sqrt{\dot{\epsilon}_{\mathrm{I}}^2+\epsilon_{\min}^2}$. The equations become

$$\zeta_{\mathrm{MC-PS}} = \frac{P(1+k_t)}{2\sqrt{\dot{\epsilon}_{\mathrm{I}}^2+\epsilon_{\min}^2}}, \tag{16}$$

$$\eta_{\mathrm{MC-PS}} = \min\left(\mu\frac{P(1+k_t)}{2}\frac{\left(1-\frac{\dot{\epsilon}_{\mathrm{I}}}{\sqrt{\dot{\epsilon}_{\mathrm{I}}^2+\epsilon_{\min}^2}}\right)}{\dot{\epsilon}_{\mathrm{II}}}, \eta_{\max}\right), \tag{17}$$

$$p_{\mathrm{MC-PS}} = \frac{1-k_t}{2}P,. \tag{18}$$

This change helps the numerical convergence (not shown). The value of $\zeta_{\max}$, $\eta_{\max}$ and $\epsilon_{\min}$ are chosen so the transition between viscous and plastic behavior takes place for deformation around $\epsilon_{\min} = 10^{-9}\,s^{-1}$.

There are four different transitions between plastic and viscous deformations with this yield curve (see the circled numbers on Figure 1):

1. In pure shear, sea ice deformation is plastic. The flow rule is vertical (non-normal to the yield curve). Note that in divergence and convergence the deformation is viscous due to regularization but smaller than $\epsilon_{\min}$.

2. In pure convergence or divergence, all the stress states are located at $\sigma_{\mathrm{I}} = -P$, $\sigma_{\mathrm{II}} = \mu(P+k_t)$ or ($\sigma_{\mathrm{I}} = k_t P = T$, $\sigma_{\mathrm{II}} = 0$), respectively. For these two stress states, there is no unique relationship between strain rate and stress state, different strain rates lead to the same stress. We see this behavior emerge clearly from the division of $\dot{\epsilon}_{\mathrm{I}}$ by the absolute value of itself in Eq. 14.

3. On the cap of the Mohr–Coulomb yield curve, strain rates are plastic (large) in convergence and viscous (small) in shear. As the stress moves from the limb (point **2**) towards the $\sigma_{\mathrm{I}}$ axis, the shear deformation decreases from $\epsilon_{\min}$ to zero. Note that on the cap of the yield curve, the flow rule is normal to the yield curve.

4. In the interior of the yield curve, the strain rates are viscous (small) in both divergence and shear. The deformation transitions from axial convergence to pure shear as the stress states move from the $\sigma_{\mathrm{I}}$ axis to the limb in both shear and divergence inside the yield curve. For small strain rates, the stresses tend to $\left(\sigma_{\mathrm{I}} = -\frac{(1-k_t)P}{2}, \sigma_{\mathrm{II}} = 0\right)$. The deformation is fully viscous.

Note that we did not apply here the truncation for high compressive stress done for the constitutive equations of the other flow rules (Sect. 2.3 and 2.4), as (1) there is no issue of flow rule directed inside the yield curve, and (2) it would move all the plastic states with convergent deformation to a state of no shear strength which would be highly unphysical and would lead to more numerical convergence issues.

https://doi.org/10.5194/egusphere-2026-1845
Preprint. Discussion started: 16 April 2026
© Author(s) 2026. CC BY 4.0 License.

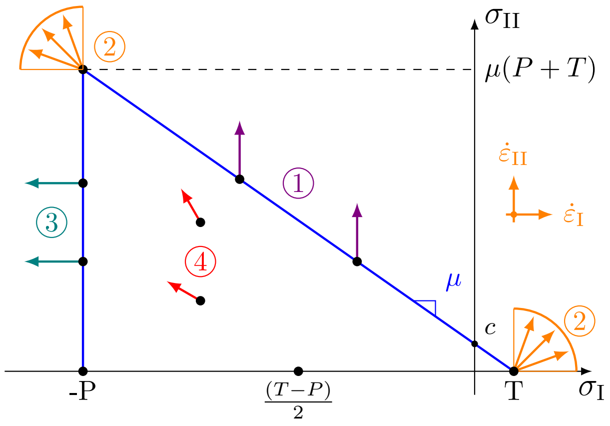

**Figure 1.** Mohr–Coulomb yield curve inspired by Ip et al. (1991) with the illustration of the four flow-rule behaviors: **1** is plastic in shear and viscous in divergence, **2** is purely plastic behavior, **3** is plastic in divergence and viscous in shear, and **4** is purely viscous.

### 2.3 Mohr–Coulomb yield curve with elliptical plastic potential (MC-E)

To obtain a yield curve with a well-defined flow rule all along the Mohr–Coulomb yield curve limbs (including at the corners ② in Figure 1), we apply the flow rule of the elliptical yield curve to the Mohr–Coulomb yield curve.

Note that the yield curve derived in this section is not built by using the yield curve and the plastic potential as in Ringeisen et al. (2021), but by setting a different $\eta$ to have a Mohr–Coulomb-shaped yield curve and $\zeta$ the same as with the elliptical yield curve with normal flow rule. We derived the constitutive equations using a plastic potential, but we were unsuccessful to use this rheology in our sea ice model, for completeness we report our derivations in Appendix B.

We start by using the $\zeta$ from the elliptical yield curve with tensile strength (König Beatty and Holland, 2010)

$$\zeta_{\mathrm{MC-E}} = \frac{P(1+k_t)}{2\Delta}, \tag{19}$$

with $\Delta$ defined as (see Eq. 9, Hibler, 1979),

$$\Delta = \sqrt{(\dot{\epsilon}_{11}+\dot{\epsilon}_{22})^2 + \frac{1}{e^2}\left[(\dot{\epsilon}_{11}-\dot{\epsilon}_{22})^2 + 4\,\dot{\epsilon}_{12}^2\right]}. \tag{20}$$

and

$$p_{\mathrm{MC-E}} = \frac{(1-k_t)}{2}P. \tag{21}$$

We use Eq. (2) and insert the constitutive equations in stress invariant space Eq. (9) so that

$$\sigma_{\mathrm{II}} = \eta\dot{\epsilon}_{\mathrm{II}} = -\sigma_{\mathrm{I}}\mu + Pk_t\mu. \tag{22}$$

Solving Eq. (22) for $\eta$ yields

$$\eta = \frac{-\sigma_{\mathrm{I}}\mu + Pk_t\mu}{\dot{\epsilon}_{\mathrm{II}}} \tag{23}$$

https://doi.org/10.5194/egusphere-2026-1845
Preprint. Discussion started: 16 April 2026
© Author(s) 2026. CC BY 4.0 License.

and after inserting Eq. (8)

$$\eta_{\mathrm{MC-E}} = \frac{\mu\left[\frac{P(1-k_t)}{2} - \zeta\dot{\epsilon}_{\mathrm{I}} + Pk_t\right]}{\dot{\epsilon}_{\mathrm{II}}}, \tag{24}$$

which can be simplified by inserting Eq. (19)

$$\eta^{\star}_{\mathrm{MC-E}} = \frac{\mu P(1+k_t)}{2}\frac{\left[1-\frac{\dot{\epsilon}_{\mathrm{I}}}{\Delta}\right]}{\dot{\epsilon}_{\mathrm{II}}}. \tag{25}$$

At the apex of the Mohr–Coulomb yield curve, as the deformation becomes directed toward convergent states, this flow rule directs post-failure deformation towards the interior of the yield curve, which implies an unphysical increase of energy instead of energy dissipation. Because this will lead to instabilities, we introduce a new limb in the yield curve by

$$\sigma_{\mathrm{II}} = \mu_c\sigma_{\mathrm{I}} + \mu_c P \tag{26}$$

which can be written as

$$\eta_{\mathrm{cap}} = \frac{\mu_c\left[\zeta\dot{\epsilon}_{\mathrm{I}} - \frac{P(1-k_t)}{2} + P\right]}{\dot{\epsilon}_{\mathrm{II}}}. \tag{27}$$

Then we use

$$\eta_{\mathrm{MC-E}} = \min\left(\eta^{\star}_{\mathrm{MC-E}}, \eta_{\mathrm{cap}}\right). \tag{28}$$

Note that $\eta$ is now uncoupled from $\zeta$ when it comes to viscous-plastic transition, unlike for the elliptical yield curve. For small deformation rates, if $\zeta$ reached its maximum $\zeta_{\mathrm{max}}$, $\eta$ does not reach a maximum. To ensure that the state is viscous we define $\eta_{\mathrm{max,MC-E}}$ as a function of $\zeta_{\mathrm{max}}$, $\eta$, and $\zeta$

$$\eta_{\mathrm{max,MC-E}} = \min\left(\zeta_{\mathrm{max}}\frac{\eta}{\zeta}, \eta_{\mathrm{max}}\right) \tag{29}$$

And then we take the minima

$$\eta = \min\{\eta_{\mathrm{MC-E}}, \eta_{\mathrm{max,MC-E}}\} \tag{30}$$

$$\zeta = \min\{\zeta_{\mathrm{MC-E}}, \zeta_{\mathrm{max}}\}. \tag{31}$$

In this way, we have plastic deformation along the Mohr–Coulomb limbs, viscous deformation inside the yield curve, and half-plastic deformations for high compressive stress, as shown in Figure 2. This rheology has a non-normal flow rule for linear limbs, except on one point, where the flow rule is perpendicular to the yield curve.

The MC-E yield curve can be used to create a Mohr–Coulomb yield curve with a quasi-shear flow rule that can be compared to the Mohr–Coulomb yield curve with a shear flow rule. To create such a flow rule, we increase the ellipse ratio to $e = 50$. The ellipse becomes very thin, and all flow rule vectors are approximately aligned with the shear direction (Figure 2b). The MC-E rheology with $e = 50$ is referred to by the acronym MC-ES.

Note that if $e \to \infty$ then from Eq. (20), $\Delta \to |\dot{\epsilon}_{\mathrm{I}}|$, and Eq. (25) and Eq. (19) become the same as the Mohr–Coulomb rheology with a non-normal shear flow rule MS-PS described in Sect. 2.2 and Ip et al. (1991).

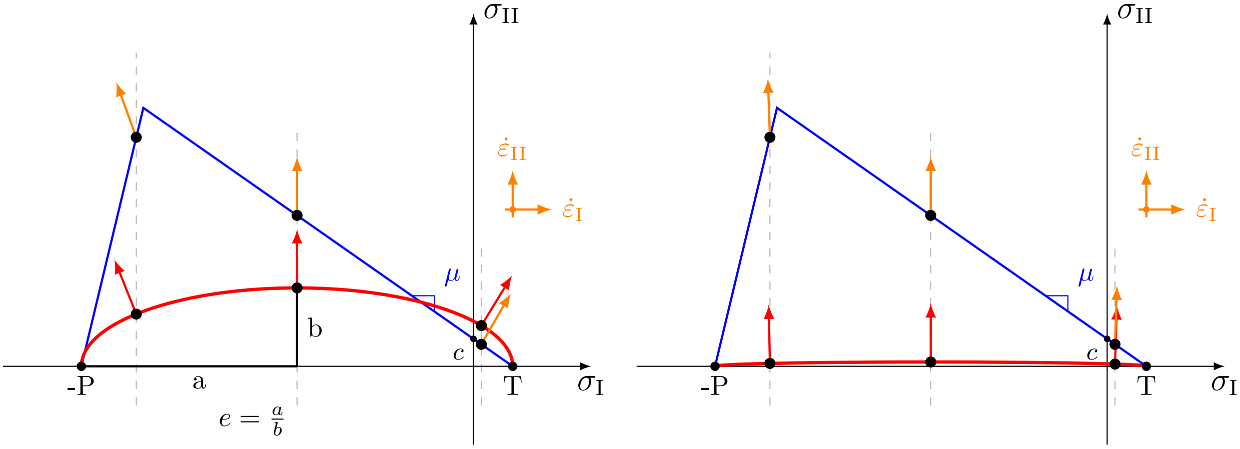

**Figure 2. (a)** Schematics of the MC-E yield curve with a plastic potential ellipse ratio $e = 2.75$. **(b)** MC-E yield curve with a plastic potential ellipse ratio $e = 50$, referred to as MC-ES. Here, both yield curves are shown with $\mu = 0.7$, and $\mu_c = 4$

## 2.4 Mohr–Coulomb yield curve with teardrop (MC-TD) and parabolic lens (MC-PL) plastic potentials

We introduce two new rheologies, both based on a Mohr–Coulomb yield curve with a non-normal flow rule: one employs a teardrop plastic potential, and the other a parabolic lens plastic potential (Figure 3). The equation of the plastic potentials is

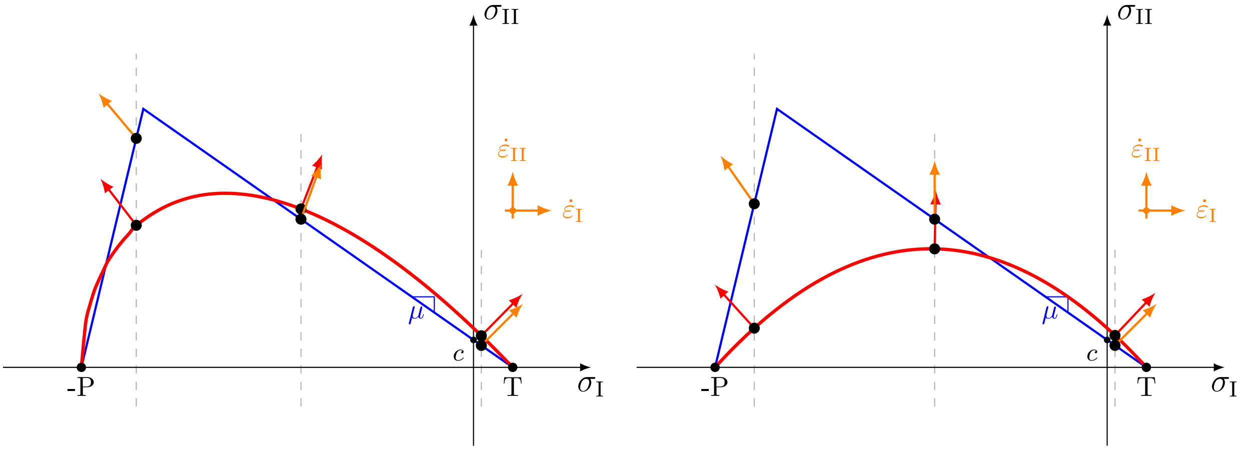

**Figure 3.** Mohr–Coulomb yield curves with a yield curve slope $\mu = 0.7$, a tensile strength factor of $k_t = 0.1$ and a compression cap with slope $\mu_c = 4$, with a Teardrop (MC-TD) and Parabolic Lens (MC-PL) plastic potentials.

185 defined by

$$G = \frac{\sigma_{\mathrm{II}}}{P} + \left(\frac{\sigma_{\mathrm{I}}}{P} - k_t\right)\left(\frac{\sigma_{\mathrm{I}}}{P} + 1\right)^q = 0, \tag{32}$$

with $q = \frac{1}{2}$ for the TD and $q = 1$ for the PL. The flow rule requirement is then that

$$\lambda \frac{\partial G}{\partial \sigma_{\mathrm{I,II}}} = \dot{\epsilon}_{\mathrm{I,II}}. \tag{33}$$

Using this, we can write that

$$\sigma_{\mathrm{I}} = \underbrace{\frac{2P}{9\dot{\epsilon}_{\mathrm{II}}}\left(\frac{\dot{\epsilon}_{\mathrm{I}}}{\dot{\epsilon}_{\mathrm{II}}} + \sqrt{\left(\frac{\dot{\epsilon}_{\mathrm{I}}}{\dot{\epsilon}_{\mathrm{II}}}\right)^2 + 3(1+k_t)}\right)}_{\zeta_{\mathrm{MC-TD}}} \dot{\epsilon}_{\mathrm{I}} - \underbrace{\frac{2-k_t}{3}P}_{p_{\mathrm{MC-TD}}}, \tag{34}$$

for the TD, and

$$\sigma_{\mathrm{I}} = \underbrace{\frac{2P}{4\dot{\epsilon}_{\mathrm{II}}}}_{\zeta_{\mathrm{MC-PL}}} \dot{\epsilon}_{\mathrm{I}} - \underbrace{\frac{1-k_t}{2}P}_{p_{\mathrm{MC-PL}}} \tag{35}$$

for the PL (see Ringeisen et al., 2023b, Sect. 2.2).

Then we use the Mohr–Coulomb criterion Eq. (1) to get, as for the MC-E rheology Eqs (22) in Sect. 2.3:

$$\eta_{\mathrm{MC-X}} = \frac{\mu\left(p_{\mathrm{MC-X}} - \zeta_{\mathrm{MC-X}}\dot{\epsilon}_{\mathrm{I}} - Pk_t\right)}{\dot{\epsilon}_{\mathrm{II}}} \tag{36}$$

where X is either TD or PL.

As for the MC-E rheology, we use the compressive cap as defined by Eq. (27) to avoid flow rules pointing inward into the yield curve. Also, we apply the viscosity maximum jointly to avoid stress states that are plastic in shear and viscous in divergence, or inversely (Eq. 30 and 31).

## 3 Experimental setup

The Mohr–Coulomb rheologies are implemented in the MIT general circulation model (MITgcm, Marshall et al., 1997) sea ice package (Losch et al., 2010). We do not use the ice thickness category scheme (e.g., Lipscomb, 2001). The model domain has dimension $L_x = 10\,\mathrm{km}$ by $L_y = 25\,\mathrm{km}$. The domain is covered with sea ice with a thickness $h = 1\,\mathrm{m}$ and concentration $A = 1$, except for two 1 km vertical bands of open water on both side of the domain(Figure 4). The southern boundary at $y = 0$ is closed with a no-slip and no flow boundary condition.

We use two numerical experiments, one to study the angles of failure and one to study the numerical convergence. These two experiments use different spatial and temporal resolutions, types of forcing (boundary or surface forcings, circled numbers on Fig. 4), and numerical convergence criteria:

1. For uni-axial loading experiments to study the angles of failure, we ramp-up a prescribed (linearly varying) ice velocity at the northern border ($y = L_y$) from $v_i = 0\,\mathrm{m\,s^{-1}}$ to $v_i = 0.1\,\mathrm{m\,s^{-1}}$ over a period of 5 s, in order to have a spatially uniform stress state in the ice field (see also Ringeisen et al., 2019). The northern boundary (with prescribed ice velocities) uses a Neumann boundary condition on ice thickness ($h = 1$m) and concentration ($A = 1$) entering the domain, while the

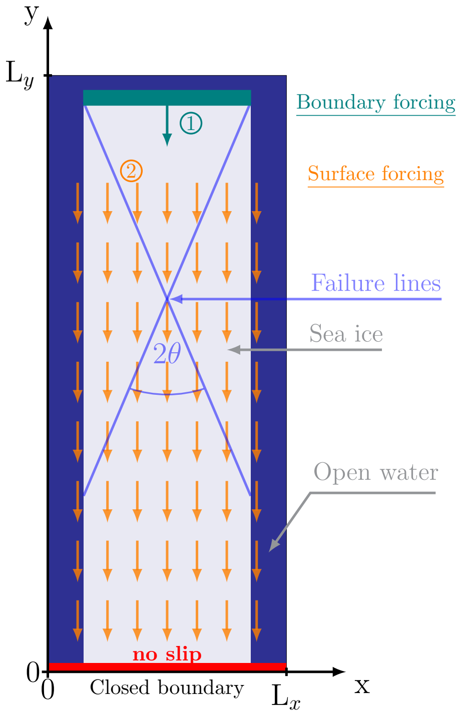

**Figure 4.** Idealized domain for the uni-axial experiment with two separate boundaries and surface forcing considered, similar to the one used in Ringeisen et al. (2023b). The orange arrows (1) represent the uniform surface wind stress used for the numerical convergence experiment. The teal area (2) represents the boundary forcing used to investigate the failure angles (Ringeisen et al., 2019). The southern boundary where a no-slip boundary condition is used is shown in red. The blue lines show the failure lines and the intersection angle equal to twice the failure angle $\theta$ .

eastern and western boundaries ($x = 0$ and $x = L_x$) we use Neumann boundary conditions (no normal gradient) on both the velocity and mass fields. The vertical bands of open water on the eastern and western boundaries are used to ensure there is no influence of the choice of boundary conditions on sea ice dynamics.

Numerically, we use a Picard solver with 1500 outer-loop iterations (or pseudo-timesteps) (Zhang and Hibler, 1997); and the linearized set of equations are solved using the Line-Successive-Relaxation (LSOR) solver with a norm ( $\varepsilon_{\mathrm{LSR}} = 10^{-11}\,\mathrm{m\,s^{-1}}$) accuracy or 1500 iterations, whichever comes first. The grid spacing in 25 m, the timestep is 0.1 s and the experiment total length is 5 s.

After failure, the angles are measured manually using the *Measure Tool* of the GNU Image Manipulation Program (GIMP, version 2.8.16, https://www.gimp.org, last accessed 2025-12-31). We used and tested a similar experimental setup extensively, see details in Ringeisen et al. (2019).

© Author(s) 2026. CC BY 4.0 License.

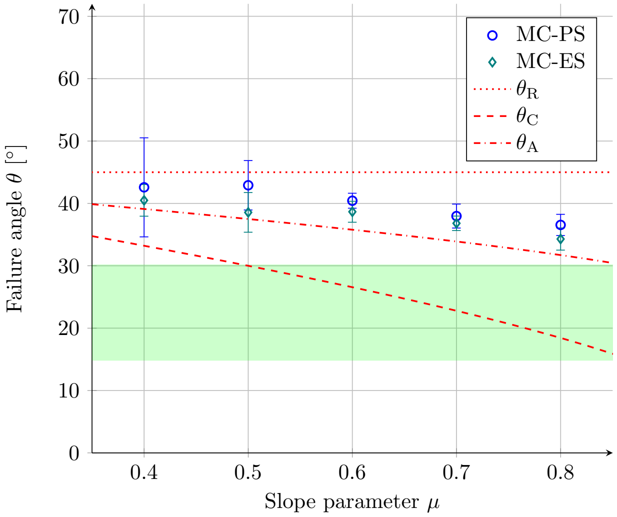

**Figure 5.** Failure angles as a function of the yield curve slopes for the MC-PS and MC-ES rheologies. The green range indicated the most common failure angles observed in the Arctic sea ice.

2. For the numerical convergence experiments (Fig 8), we increase the grid spacing from 25 m to 1 km and accordingly the timestep (from 0.1 s to 10 s) and the total integration time (from 5 s to 1000 s), in line with current high-resolution coupled ice-ocean standards. Moreover, we use a uniform surface stress of $0.15\,\mathrm{N\,m^{-2}}$ – as opposed to a specified velocity at the boundary. Also, a band of 1 km width is left ice free at the northern boundary to avoid the non-physical no-normal flow boundary condition for offshore winds.

   Numerically, we increase the numerical solver settings to 15 000 outer-loop iterations , and a maximum of 15 000 LSOR iterations. For reference, we repeated all experiments with a typical convergence criteria for pan-arctic simulations, i.e., 10 outer-loop iterations, $\varepsilon_\mathrm{LSR} = 10^{-6}\,\mathrm{m\,s^{-1}}$ or 200 maximum LSOR iterations (whichever come first).

For all the experiments, a tensile strength factor of 5% (i.e., $k_t = 0.05$) is used if the value is not precised.

## 4 Results

### 4.1 Failure angles

The failure angles of the MC-PS and MC-ES rheologies are similar, and follow closely the Arthur's angle (Figure 5). However, the failure angles are too large and do not reach the 15° to 30° range of the observations (Ringeisen et al., 2023a). The MC-ES rheology is a good replacement for the MC-PS rheology, as it gives the same failure angles but with a better numerical convergence, see Sect. 4.2 below. The main difference between these two rheologies is the viscous-plastic transition.

For the MC-E rheology, We study the evolution of the failure angles with the parameters $e$ and $\mu$. In a first step, the yield curve is kept the same (i.e., the yield curve slope $\mu$ is constant) and we study the effect of changing the plastic potential or ellipse ratio $e$). The failure angles change with the flow rule orientation (as a function of $e$) in contradiction with the Coulombic theory of the internal angle of friction, which does not account for the orientation of the flow rule but only the slope of the yield curve (Figure 6a). However, the angles do not follow the predictions given by the Roscoe angles either. The simulated angles agree best with the Arthur's angle $\theta_A$ (Equation 5), although even the Arthur's angle underestimates the failure angles slightly. For $e \approx 1.35$, the flow rule is normal at this precise point of uni-axial compressive stress (the point where all three predictions are the same), and the simulations develop clear failure lines with a very small variation range (Figure 6a, second data point from the left).

In the second step, the plastic potential is kept constant (i.e., $e$ is constant), and we change the yield curve slope $\mu$. For two different values for the plastic potential ellipse ratio ($e = 1.4$ and $e_G = 4.0$), the modeled angles show a good agreement with the Arthur's angle. The failure angles are influenced by both the yield curve shape and the flow rule direction (Figure 6b). As for Fig. 6a, and for both values of $e$, Arthur's angle underestimates the angles slightly. With $e = 1.4$, no failure angles are shown for $\mu = 0.3$ and $\mu = 0.4$ because there is no clear failure pattern. For these two cases, no angles could be derived from Roscoe's angle predictions because the absolute value of the slope of the plastic potential is greater than 1. It appears to be necessary that both Coulomb and Roscoe angles are defined to create a failure line.

As with the other Mohr–Coulomb rheologies, the failure angles with MC-TD and MC-PL rheologies also follow the Arthur failure angles predictions (Figure 7). Both MC-TD and MC-PL can also create smaller failure angles in uniaxial compression, that fall into the observed range. The numerical convergence with the MC-TD and MC-PL rheologies was harder to attain when compared to the MC-E rheology, visible by the large spread of angles measured. Also, we experience more convergence issues with these two rheologies especially when the tensile strength factor $k_t$ is smaller or equal to $5\%$. These convergence and stability issues can probably be traced back to the pointy tips of both TD and PL plastic potentials where differentiability is lost (Ringeisen et al., 2023b). For this reason, to have the failure point further away from the problematic area of the yield curve, we used here a higher tensile factor $k_t = 0.1$.

### 4.2 Numerical convergence

The numerical convergence of sea-ice dynamics solvers is delicate (Lemieux et al., 2010; Ringeisen et al., 2021; Kimmritz et al., 2016). More complicated rheologies (non-normal flow rules, shapes with kinks, etc...) tend to lead to poorer convergence (Ringeisen et al., 2023b). We see the same here, where the fastest convergence with respect to an L2-norm of the residuals is achieved for the elliptic yield curve with normal flow rule (Figure 8a, blue line). For all Mohr–Coulomb rheologies, the solver reduces the residuals by 1–2 orders of magnitude and then stalls, indicating a noisy solution.

If we use a less stringent convergence criterion (10 non-linear iterations, 200 linear iterations, LSR convergence criteria of $\Delta u = 10^{-6}\,\mathrm{m\,s^{-1}}$), the convergence properties of the Mohr–Coulomb rheologies are similar to that of the elliptical yield curve (Figure 8, right panel). The difference of improvement between the hard and relaxed convergence criteria for the elliptical yield curve and the Mohr–Coulomb rheologies suggest that this rheology may be ill-posed. In previous studies, stress states lying

https://doi.org/10.5194/egusphere-2026-1845
Preprint. Discussion started: 16 April 2026
© Author(s) 2026. CC BY 4.0 License.

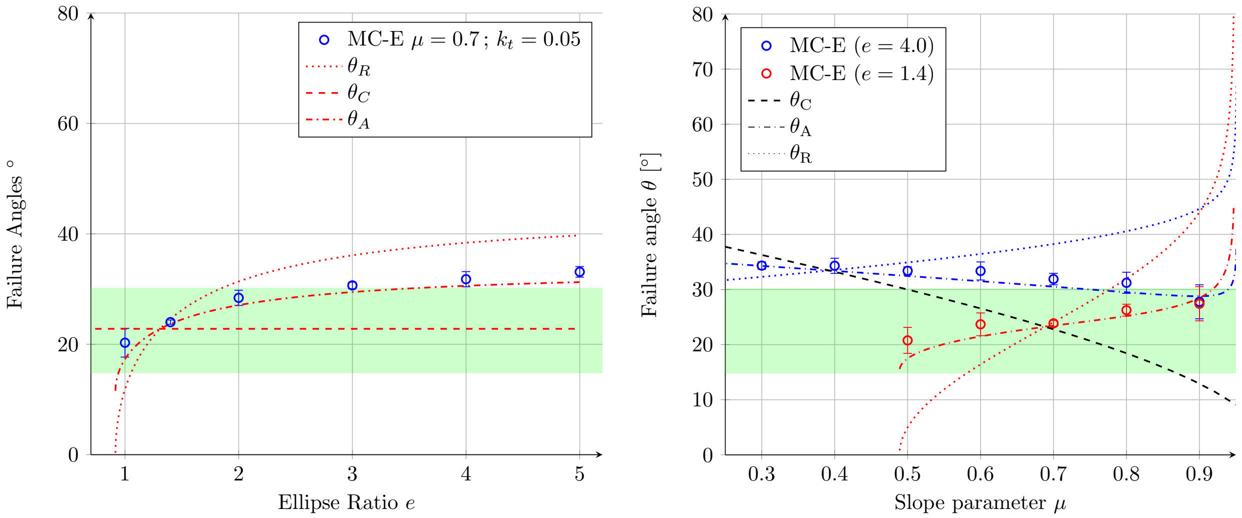

**Figure 6. (a)** Average failure angles as a function of the plastic potential ellipse ratio $e$, in blue, with the theoretical predictions, in red. The ranges show the $2\sigma$ deviation. With a normal flow rule, at the intersection of the predictions, the variations are minimal. The shaded green area on the graph shows the range of failure angles in Arctic observations. **(b)** Average failure angles as function of the yield curve slope $\mu$ for $e = 1.4$ (red) and $e = 4.0$ (blue). The theoretical predictions of the Roscoe angles and the Arthur's angle are shown in the corresponding color. The predictions from the Coulomb angle are the same for both cases and are shown in black. The error ranges are the $2\sigma$ deviation of the measure angles. With a normal flow rule, at the intersection of the predictions, the angle variations are minimal. The shaded green area on the graph shows the range of failure angles in observations.

outside of the yield curve was considered an indication of poor numerical convergence (e.g., Zhang and Rothrock, 2005); we do not observe this behavior in any of the simple experiments using the Mohr-Coulomb yield curve with both the strict and the usual convergence criteria (not shown).

## 5 Discussion

The results comparing the MC-PS and MC-ES rheologies show that numerical convergence is better when the flow rule of a sea ice VP model is fully plastic, in both convergence/divergence and shear. Our analysis of the formulation and behavior of the MC-PS formulation shows that numerical convergence is much better when we avoid a mix of viscous and plastic state and it could be the reason why the Mohr–Coulomb formulation of Ip et al. (1991) needs a very small angle of friction ($\phi = 0.01$) to reach an acceptable numerical convergence (Lemieux and Dupont, 2020). The MC-ES numerical convergence is better. However, even for the MC-ES rheology, the failure angles spread considerably: the flow rule is non-normal so the convergence is more difficult to achieve than with a normal flow rule (Ringeisen et al., 2021). A downside of the MC-ES rheology is that while it approximates a pure shear flow rule, the deformation in convergence and divergence is still non-zero. A pure shear

https://doi.org/10.5194/egusphere-2026-1845
Preprint. Discussion started: 16 April 2026
© Author(s) 2026. CC BY 4.0 License.

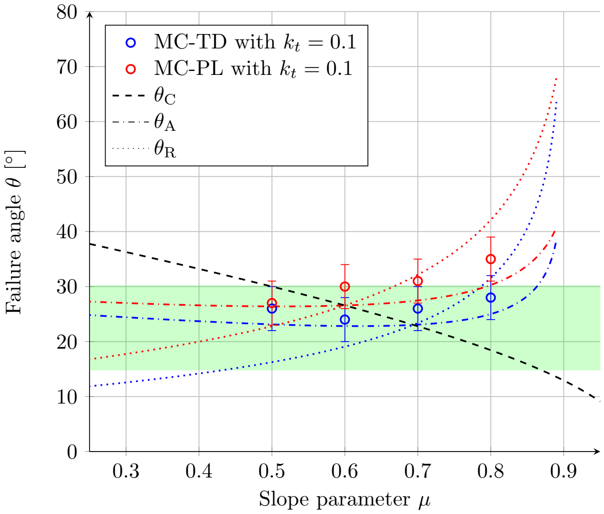

**Figure 7.** Failure angles in uniaxial compression for the MC-TD (in red) and MC-PL (in blue) as a function of the yield curve slope $\mu$. The theoretical failure angles are shown from Coulomb (dotted), Roscoe (dashed), and Arthur (dash-dotted).

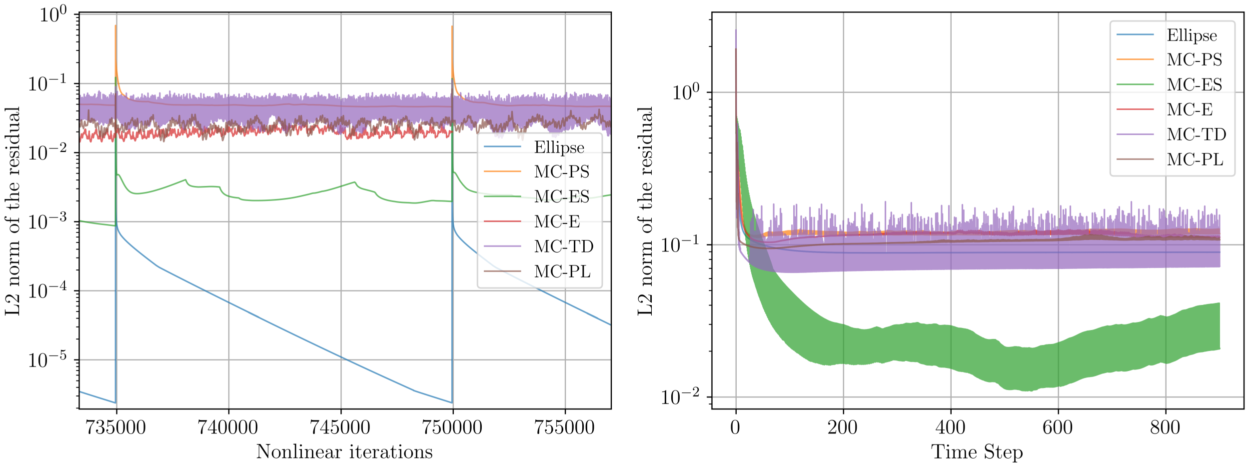

**Figure 8.** Numerical convergence of the rheological models. (**left panel**) Residual of the momentum equation (scaled, i.e., normalized by the domain size) as function of the non-linear iterations, for 1 timesteps after 49 timesteps. (**right panel**) Residual of the momentum equation (scaled) as function of the timesteps for a simulation of 1000 timesteps with a convergence criteria usual for climate models.

https://doi.org/10.5194/egusphere-2026-1845
Preprint. Discussion started: 16 April 2026
© Author(s) 2026. CC BY 4.0 License.

flow rule could be conceptually interesting but it would require an incompressible formulation in which the divergence is set to zero explicitly (Rothrock, 1975). This is beyond the scope of the present work and is therefore left for future work.

The failure angles with the Mohr–Coulomb yield curve with all the different plastic potentials follow the Arthur's angle (Arthur et al., 1977; Vermeer, 1990). This combined theory can be called a macroscopic angle of friction that results from the equal and joint influence of a microscopic angle of friction and an angle of dilatancy (Balendran and Nemat-Nasser, 1993; Tremblay and Mysak, 1997). In Ringeisen et al. (2019, Figure 4) and Ringeisen et al. (2021, Figure 3), we developed rationals for the Coulomb and Roscoe angles, respectively, using the Mohr's circle of stresses and the shape of the yield curve and plastic potential. We are unsure why the angle of failure is the Arthur's angle and not the Roscoe or Coulomb angles. We speculate that the Arthur's angle leads to the most efficient dissipation of energy. The dissipation of energy as a function of the orientation and the parameters of the rheologies remains to be investigated.

All Mohr–Coulomb yield curves examined in this work present significant challenges for numerical convergence. This contrasts with the elliptical yield curve, for which convergence is readily achieved with both normal (Zhang and Hibler, 1997) and, in a lesser way, with non-normal (Ringeisen et al., 2021) flow rules, as well as with the teardrop yield curve (Ringeisen et al., 2023b). Increasing the number of (linear or non-linear) iterations of the solver helps but does not resolve this issue. The numerical convergence properties of existing rheological formulations as well as the new formulations proposed here, remain problematic. Nevertheless, we consider it important to highlight these issues to encourage further advances in numerical solvers and in the design of more stable rheological models. For example, the recent analysis of the elliptical yield curve (Brandt et al., 2022; Binz et al., 2025) could be extended to more yield curves/flow rule configurations. In practice, sea ice models used in climate simulations are practically never iterated to convergence because of the computational cost, and other errors dominate the momentum equation (e.g., coupling) (Lemieux and Tremblay, 2009; Kimmritz et al., 2016, e.g.,). Instead, a fixed small number of iterations is often used (e.g., Zhang and Hibler, 1997, suggest 15). This problem is not unique to sea ice modeling, the Mohr–Coulomb yield curve with non-normal (or non-associative) flow rule is showing same issues in the field of soil modeling. Several studies have looked into possible solutions, for example using a Cosserat formulation that allows rotation (de Borst et al., 2022) or a smooth approximation of the Mohr–Coulomb limbs (Abbo et al., 2011; Abbo and Sloan, 1995), which could be explored for sea ice as well.

Using an MC-E, MC-TD, and MC-PL rheology reduces the angles of failure of conjugate faults in sea ice models below the 30° limit of the elliptical yield curve rheological model (Ringeisen et al., 2019). We note that using a small ellipse ratio ($e \leq 1.0$) is counter-productive, as the area of the plastic potential where the magnitude of the slope is lower than one – allowing failure to be simulated – reduces. As shown using the Mohr's circle in the appendix of Ringeisen et al. (2019), a failure can be only created if the slope of the yield curve and the plastic potential are inside the range $[-1,1]$. We observe this behavior in Figure 6b, where no failure pattern could be found for $\mu < 0.5$ when $e = 1.4$.

The MC-E rheology appears as a suitable candidate for high-resolution sea ice modeling with realistic failure patterns. It features a well-defined flow rule that captures divergent behavior with open-water creation, convergent behavior associated with ridge formation, and the full range in between, as observed (Stern et al., 1995; Bouchat and Tremblay, 2017). The most common and well-established viscous-plastic rheology with an elliptical yield curve and normal flow rule suffers from several

https://doi.org/10.5194/egusphere-2026-1845
Preprint. Discussion started: 16 April 2026
© Author(s) 2026. CC BY 4.0 License.

issues, most notably, an overestimation of the LKFs intersection angles (Ringeisen et al., 2019). This could potentially be addressed with the MC-E rheology: The angle of failure and the post-failure deformation are partially decoupled from the yield curve, hence giving more control over the behavior of the rheology. However, more tests are necessary to assess how the Mohr–Coulomb yield curves would perform in pan-Arctic simulations (Bouchat et al., 2022; Hutter et al., 2022) apart from the issues of numerical convergence. A recent study, Lemieux et al. (2025) showed that using the elliptical yield curve with a non-normal flow rule does not seem to change the failure angles significantly in pan-arctic simulations, but there was a clear change of the deformation along the LKFs.

## 6 Conclusions

The Mohr–Coulomb yield criterion is a classical representation of stress for models of granular materials. Numerical tests with four formulations of the Mohr–Coulomb criterion for the VP sea ice rheological models with different plastic potentials (hence different flow rules) show that the way the flow rule is defined is important for the numerical convergence of the momentum equation. It appears to be better to avoid stress states with mixed behaviors (plastic in shear and viscous in convergence, or vice versa). Mohr–Coulomb yield curves with elliptical, teardrop, and parabolic lens plastic potential allow for failure angles that can be close to the observed range of $15-30°$ (Ringeisen et al., 2023a). For the elliptical plastic potential, with a slope $\mu \in [0.6, 0.8]$ (Schulson, 2004; Weiss and Schulson, 2009), this is achieved by having a plastic potential ellipse ratio $e_G \in [1.2, 2]$. The failure angles are both influenced by the shape of the yield curve and the shape of plastic potential, giving LKFs failure angles close to the Arthur's angle (Arthur et al., 1977; Vardoulakis, 1989).

The VP rheological model for sea ice is well established in climate modeling. In comparison to implementing completely new rheological models (e.g., brittle models) or approaches (discrete element models) to improve the sea-ice component in a climate model, it is still an interesting alternative to improve the VP model. Here we demonstrated for the example of overestimated failure angles (Hutter et al., 2022; Ringeisen et al., 2023a), how relatively small changes of introducing a new yield curve and plastic potential can fix a persistent problem in VP models. However, poor numerical convergence and increased computer load could be an obstacle. The mathematical properties (e.g., well-posedness) of the VP rheology is currently still subject of study (e.g., Brandt et al., 2022; Chatta et al., 2023) and we hope that it will lead to improved rheological formulation in the future.

## Appendix A: Derivation of the MC-PS constitutive equations

In this appendix, we are giving the detailed derivations of the MC-PS rheology. The derivation of the Mohr–Coulomb with pure shear (MC-PS) rheology is not presented in Ip et al. (1991) and other previous studies. As the method used to derive the constitutive equation can lead to some issues but also highlight special properties of the rheology, we wanted to be as exhaustive as possible and explored different possible derivations, reaching the exact same equations. In the following, we present four different ways to derive the constitutive equations for the MC-PS yield curve that all give the same equation:

1. From Eqs (8–9), $p = (1-k_t)P/2$ (Hibler, 1979; König Beatty and Holland, 2010) and considering the yield criterion in compression ($\sigma_{\mathrm{I}} = -P$ when $\dot{\epsilon}_{\mathrm{I}} < 0$, and $\sigma_{\mathrm{I}} = 0$ when $\dot{\epsilon}_{\mathrm{I}} > 0$) and shear (Eq 1), we have,

$$\zeta_{\mathrm{MC-PS}} = \frac{P(1+k_t)}{2|\dot{\epsilon}_{\mathrm{I}}|}, \tag{A1}$$

$$\eta_{\mathrm{MC-PS}} = \frac{\mu\left(\frac{P(1+k_t)}{2} - \zeta\dot{\epsilon}_{\mathrm{I}}\right)}{\dot{\epsilon}_{\mathrm{II}}}, \tag{A2}$$

where

$$p_{\mathrm{MC-PS}} = \frac{1-k_t}{2}P, \tag{A3}$$

2. Eqs. (A1–A3) can also be derived directly from the constitutive equations (7), first by assuming pure shear deformation (dilatation or $\delta = 0$, and $\zeta = 0$) along two failure lines at angles plus and minus $\pi/4 - \phi/2$ from the main loading axis as per Mohr–Coulomb failure criterion (see Tremblay and Mysak, 1997, for details),

$$\sigma_{ij} = 2\eta\dot{\epsilon}_{ij} - \eta\dot{\epsilon}_{\mathrm{I}}\delta_{ij} + p\delta_{ij}, \tag{A4}$$

with

$$\eta = \frac{\mu(p + k_t P)}{2\dot{\epsilon}_{\mathrm{II}}}, \tag{A5}$$

and write $p$ as a step function going from $\sigma_{\mathrm{I}} = -P$ to $\sigma_{\mathrm{I}} = T = k_t P$ at $\dot{\epsilon}_{\mathrm{I}} = 0$, (see Fig. 1)

$$p = \left((1-k_t) - (1+k_t)\frac{\dot{\epsilon}_{\mathrm{I}}}{|\dot{\epsilon}_{\mathrm{I}}|}\right)\frac{P}{2}. \tag{A6}$$

In this formulation, $\zeta$ appears naturally, resulting in the same Eq. (A1-A3)

$$\zeta_{\mathrm{MC-PS}} = \frac{P(1+k_t)}{2|\dot{\epsilon}_{\mathrm{I}}|} \tag{A7}$$

$$\eta_{\mathrm{MC-PS}} = \frac{\mu\left(\frac{P(1+k_t)}{2} - \zeta\dot{\epsilon}_{\mathrm{I}}\right)}{\dot{\epsilon}_{\mathrm{II}}} \tag{A8}$$

$$p_{\mathrm{MC-PS}} = \frac{1-k_t}{2}P \tag{A9}$$

for the general constitutive equation Eq. (7). In the above equation, the $\dot{\epsilon}_{\mathrm{I}}$-dependent and independent terms are the bulk viscosity and the pressure term ($p$), respectively. Capping the denominator to a minimum value of $\dot{\epsilon}_{\mathrm{I}}$ transforms the step function into a linear transition over a finite range (-$\dot{\epsilon}_{\mathrm{I}}$ : $\dot{\epsilon}_{\mathrm{I}}$), enabling the use of standard (efficient) numerical methods to solve for the velocity field without having the solve for the pressure independently using a Poisson equation (Flato and Hibler, 1992; Tremblay and Mysak, 1997).

3. We can also use a plastic potential methods as used in Ringeisen et al. (2021). As described in Sect. 2.2, the plastic stress states are grouped together at the tips of the Mohr–Coulomb yield curve and we cannot represent them with a plastic

potential (see behavior **2** on Fig. 1). However, we can define the flow rule and stress along Mohr–Coulomb limbs of the yield curve where $\zeta = \zeta_{\max}$ by choosing the appropriate plastic potential. We use the Mohr–Coulomb yield curve as defined by Eq. (1) and we define the plastic potential as

$$G = \frac{1}{2\dot{\epsilon}_{\mathrm{II}}\zeta_{\max}}\left(\sigma_{\mathrm{I}} - \frac{(1-k_t)}{2}P\right)^2 + \sigma_{\mathrm{II}} \tag{A10}$$

with the flow rule conditions

$$\lambda\frac{\partial G}{\partial \sigma_{\mathrm{I,II}}} = \dot{\epsilon}_{\mathrm{I,II}} \tag{A11}$$

where $\lambda > 0$. Using these conditions we obtain

$$\zeta_{\mathrm{MC-PS}} = \zeta_{\max} \tag{A12}$$

$$\eta_{\mathrm{MC-PS}} = \frac{\mu\left(\frac{P(1+k_t)}{2} - \zeta_{\max}\dot{\epsilon}_{\mathrm{I}}\right)}{\dot{\epsilon}_{\mathrm{II}}} \tag{A13}$$

$$p_{\mathrm{MC-PS}} = \frac{1-k_t}{2}P \tag{A14}$$

Note that the proposed plastic potential function $G$ (Eq. A10) is highly unusual, as it contains the shear strain rate $\dot{\epsilon}_{\mathrm{II}}$. It would mean that $G$ changes shape as the shear strain rates change. This can explain the complex behavior of this yield curve, present in Sec. 2.2 and its poor performance in simulations.

4. We can finally use the Mohr–Coulomb yield curve with an elliptical plastic potential by making the ellipse ratio tend to infinity, see the last paragraph of Sect. 2.3.

It is important here to compute $\zeta$ and apply the viscous capping $\zeta_{\max}$ before computing $\eta$, because it is the capping that creates the Mohr–Coulomb limbs (see behavior **1** on Fig. 1).

## Appendix B: Mohr–Coulomb yield curve with an elliptical plastic potential - alternative derivation

In this appendix section, we describe an unsuccessful attempt to derive a Mohr–Coulomb yield curve with an elliptical plastic potential. We want to document this derivation to report a negative result, avoid useless replication in the future, and stimulate discussion around the derivation of sea ice rheologies.

We want to derive a constitutive equation for sea ice based on a Mohr–Coulomb failure criterion and a plastic potential. Given the stress invariants $\sigma_{\mathrm{I}}$ and $\sigma_{\mathrm{II}}$, the Mohr–Coulomb failure criterion is expressed as

$$\sigma_{\mathrm{II}} = -\mu\sigma_{\mathrm{I}} + c = -\mu\sigma_{\mathrm{I}} + \mu P k_t, \tag{B1}$$

where $\mu$ is the coefficient of friction, and the cohesion $c$ is expressed as $\mu T$ with the tensile strength $T = k_t P$. $P$ is the ice strength. Following Ringeisen et al. (2021), the flow rule is defined based on an elliptical plastic potential given by

$$G = [2\sigma_{\mathrm{I}} + (1-k_t)P]^2 + 4e^2\sigma_{\mathrm{II}}^2 - (1+k_t)^2P^2. \tag{B2}$$

https://doi.org/10.5194/egusphere-2026-1845
Preprint. Discussion started: 16 April 2026
© Author(s) 2026. CC BY 4.0 License.

Assuming a normal flow rule with respect to the plastic potential, we can write

$$\lambda \frac{\partial G}{\partial \sigma_{\mathrm{I}}} = \dot{\epsilon}_{\mathrm{I}} \text{ and } \lambda \frac{\partial G}{\partial \sigma_{\mathrm{II}}} = \dot{\epsilon}_{\mathrm{II}} \tag{B3}$$

and solve for the unknown flow rate $\lambda > 0$ an unknown to find, and the stress invariants based on three equations (B1,B3).

Differentiating equation (B2) with respect to $\sigma_{\mathrm{I}}$ and $\sigma_{\mathrm{II}}$ yields

$$4\lambda(2\sigma_{\mathrm{I}} + (1-k_t)P) = \dot{\epsilon}_{\mathrm{I}} \text{ and } 8\lambda e^2 \sigma_{\mathrm{II}} = \dot{\epsilon}_{\mathrm{II}}. \tag{B4}$$

Reordering gives expressions for the stress invariants

$$\sigma_{\mathrm{I}} = \frac{\dot{\epsilon}_{\mathrm{I}}}{8\lambda} - \frac{(1-k_t)}{2}P \text{ and } \sigma_{\mathrm{II}} = \frac{\dot{\epsilon}_{\mathrm{II}}}{8\lambda e^2}. \tag{B5}$$

After inserting Eqs (B5) in Eq. (B1), we can write

$$\frac{\dot{\epsilon}_{\mathrm{II}}}{8\lambda e^2} = -\frac{\mu \dot{\epsilon}_{\mathrm{I}}}{8\lambda} + \mu \frac{(1+k_t)P}{2}, \tag{B6}$$

which can be rearranged as

$$\lambda \Delta = \mu e^2 (1+k_t) P, \tag{B7}$$

with

$$\Delta = \dot{\epsilon}_{\mathrm{II}} + \mu e^2 \dot{\epsilon}_{\mathrm{I}}. \tag{B8}$$

The flow rate $\lambda$ is therefore

$$\lambda = \frac{\Delta}{(1+k_t)\mu e^2 P}. \tag{B9}$$

We use

$$\sigma_{ij} = 2\eta \dot{\epsilon}_{ij} + [\zeta - \eta]\dot{\epsilon}_{kk}\delta_{ij} - p\delta_{ij} \tag{B10}$$

which we can be rewritten for the stress invariants as

$$\sigma_{\mathrm{I}} = \zeta \dot{\epsilon}_{\mathrm{I}} - p \text{ and } \sigma_{\mathrm{II}} = 2\eta \dot{\epsilon}_{\mathrm{II}}. \tag{B11}$$

Combining with Eqs (B5) yields

$$\zeta = \frac{1}{8\lambda} = \frac{\mu e^2 (1+k_t) P}{2\Delta}, \tag{B12}$$

$$\eta = \frac{1}{8\lambda e^2} = \frac{\mu (1+k_t) P}{2\Delta} = \frac{\zeta}{e^2}, \tag{B13}$$

$$p = \frac{1-k_t}{2} P \tag{B14}$$

https://doi.org/10.5194/egusphere-2026-1845
Preprint. Discussion started: 16 April 2026
© Author(s) 2026. CC BY 4.0 License.

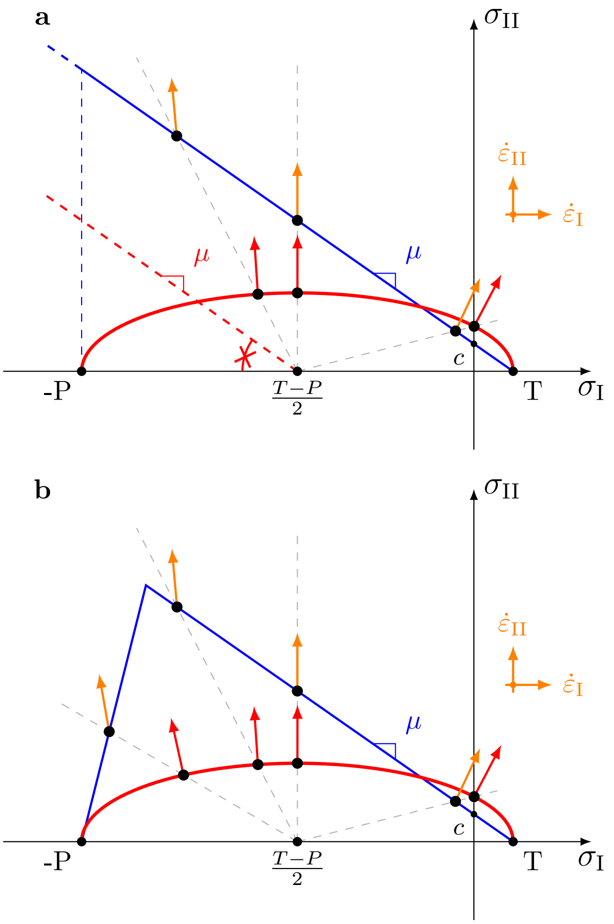

**Figure B1.** **(a)** MC-E rheology from using an elliptical plastic potential G, as derived in App. B. The angle shown in red denotes the part of the plastic potential that cannot be represented on the Mohr–Coulomb yield curve. **(b)** MC-E rheology from using an elliptical plastic potential G with the proposed compressive cap with $\mu_c = 4$. For both **(a)** and **(b)**, we use $\mu = 0.7$, $k_t = 0.1$, and $e = 2$.

There is the immediate problem that $\lambda < 0$ is possible because $\Delta$ in Eq (B8) is not positive definite. If $\lambda < 0$ then the viscosities can become negative, and the viscosity terms, per definition an sink of energy by dissipation, will become an energy source, leading to instabilities.

As explained in the corrigendum of Ringeisen et al. (2021), the flow rule from the elliptical plastic potential does not move along a line with constant $\sigma_{\mathrm{I}}$ onto the yield curve, but it moves along a line that passes through the center of the ellipse at $\sigma_{\mathrm{I}} = \frac{1+k_t}{2}P$ and $\sigma_{\mathrm{II}} = 0$. Hence, for a Mohr–Coulomb yield curve, there is a part of the plastic potential that cannot fall onto the yield curve, namely when the slope of the line passing by the center of the ellipse is $\leq \mu$ (Figure B1).

© Author(s) 2026. CC BY 4.0 License.

The MC-E yield curve derived in Sect. 2.3 does not have this problem because the bulk viscosity $\zeta$ is kept the same as the elliptical yield curve with normal flow rule and only the shear viscosity $\eta$ is changed to create a Mohr–Coulomb yield curve shape.

The MC-TD and MC-PL rheologies derived in Sect. 2.4 also do not suffer from this problem as their formulation is based on $l = \frac{\dot{\epsilon}_{\mathrm{I}}}{\dot{\epsilon}_{\mathrm{II}}}$, so the bulk viscosity of MC-TD and MC-PL are also the same as the bulk viscosity of the Teardrop and Parabolic lens yield curves with a normal flow rule (Ringeisen et al., 2023b).

To solve these issues, we can use a compressive cap, as done in Sect. 2.3 and 2.4. The equations of the cap would then become

$$\Delta_c = \mu_c e^2 \dot{\epsilon}_{\mathrm{I}} - \dot{\epsilon}_{\mathrm{II}} \tag{B15}$$

$$\zeta_c = \frac{\mu_c e^2 (1+k_t) P}{2\Delta_c}, \tag{B16}$$

$$\eta_c = \frac{\mu_c (1+k_t) P}{2\Delta_c} = \frac{\zeta_c}{e^2}, \tag{B17}$$

$$p = \frac{1-k_t}{2} P \tag{B18}$$

and the cap would be applied as

$$\zeta = \min(\zeta, \zeta_c), \tag{B19}$$

$$\eta = \min(\eta, \eta_c). \tag{B20}$$

This solution is shown in Fig. B1b. Using this compressive cap would work, however, the presence of the two minimum functions makes it unusually complex to implement and slow to use in pan-Arctic simulations due to convergence issues. It is worth mentioning that the advantage of this rheology is that the viscous behavior is very easily implemented. Applying the maximum $\zeta_{\max}$ on $\zeta$ immediately translated to a maximum on $\eta$ of $\eta_{\max} = \frac{\zeta_{\max}}{e^2}$, as for the elliptical yield curve (Hibler, 1979). Unfortunately, all tests using this formulation in MITgcm have been unsuccessful and further exploration is outside of the scope of this manuscript.

*Code and data availability.* The MC-PS rheologies are implemented in the sea ice package of the MIT general circulation model, or MITgcm (Marshall et al., 1997; Losch et al., 2010) and published the MITgcm 67z (Campin et al., 2021). The version of the MC-E, MC-TD and MC-PL rheologies used are implemented in MITgcm in the authors release published on Zenodo (Campin et al., 2026).

## Acknowledgments

The authors thank Amelie Bouchat and Mathieu Plante for discussions about the derivation of a Mohr–Coulomb yield curve for the sea ice VP rheological model.

## Financial support

This project has been supported by the Deutsche Forschungsgemeinschaft (DFG) through the International Research Training Group “Processes and impacts of climate change in the North Atlantic Ocean and the Canadian Arctic” (grant no. IRTG 1904 ArcTrain). This project contributes to the Natural Science and Engineering Research Council - Discovery Program and the Grant & Contributions from Environment and Climate Change Canada awarded to Tremblay. The author(s) would like to thank the Isaac Newton Institute for Mathematical Sciences, Cambridge, for support and hospitality during the programme SIP Follow on: Mathematics of sea ice in the twenty-first century, where work on this paper was undertaken. This work was supported by EPSRC grant EP/K032208/1.

*Author contributions.* DR, BT, JFL, and ML derived the different Mohr–Coulomb yield curve formulations. DR and ML implemented the rheologies in MITgcm. DR ran the experiments, interpreted the results, and wrote the original draft. All the authors edited the manuscript.

*Competing interests.* The authors declare that they have no conflict of interest

https://doi.org/10.5194/egusphere-2026-1845
Preprint. Discussion started: 16 April 2026
© Author(s) 2026. CC BY 4.0 License.

## References

Abbo, A. J. and Sloan, S. W.: A smooth hyperbolic approximation to the Mohr-Coulomb yield criterion, Computers & Structures, 54, 427–441, https://doi.org/10.1016/0045-7949(94)00339-5, 1995.

Abbo, A. J., Lyamin, A. V., Sloan, S. W., and Hambleton, J. P.: A C2 continuous approximation to the Mohr–Coulomb yield surface, International Journal of Solids and Structures, 48, 3001–3010, https://doi.org/10.1016/j.ijsolstr.2011.06.021, 2011.

Arthur, J. R. F., Dunstan, T., Al-Ani, Q. a. J. L., and Assadi, A.: Plastic deformation and failure in granular media, Géotechnique, 27, 53–74, https://doi.org/10.1680/geot.1977.27.1.53, 1977.

Balendran, B. and Nemat-Nasser, S.: Double sliding model for cyclic deformation of granular materials, including dilatancy effects, Journal of the Mechanics and Physics of Solids, 41, 573–612, https://doi.org/10.1016/0022-5096(93)90049-L, 1993.

Binz, T., Brandt, F., and Hieber, M.: Interaction of geophysical flows with sea ice dynamics, Nonlinear Differential Equations and Applications NoDEA, 33, 35, https://doi.org/10.1007/s00030-025-01169-w, 2025.

Bouchat, A. and Tremblay, B.: Using sea-ice deformation fields to constrain the mechanical strength parameters of geophysical sea ice, Journal of Geophysical Research: Oceans, pp. n/a–n/a, https://doi.org/10.1002/2017JC013020, 2017.

Bouchat, A., Hutter, N., Chanut, J., Dupont, F., Dukhovskoy, D., Garric, G., Lee, Y. J., Lemieux, J.-F., Lique, C., Losch, M., Maslowski, W., Myers, P. G., Ólason, E., Rampal, P., Rasmussen, T., Talandier, C., Tremblay, B., and Wang, Q.: Sea Ice Rheology Experiment (SIREx): 1. Scaling and Statistical Properties of Sea-Ice Deformation Fields, Journal of Geophysical Research: Oceans, 127, e2021JC017 667, https://doi.org/10.1029/2021JC017667, _eprint: https://onlinelibrary.wiley.com/doi/pdf/10.1029/2021JC017667, 2022.

Brandt, F., Disser, K., Haller-Dintelmann, R., and Hieber, M.: Rigorous Analysis and Dynamics of Hibler's Sea Ice Model, Journal of Nonlinear Science, 32, 50, https://doi.org/10.1007/s00332-022-09805-w, 2022.

Campin, J.-M., Heimbach, P., Losch, M., Forget, G., Edhill3, Adcroft, A., Amolod, Menemenlis, D., Dfer22, Hill, C., Jahn, O., Scott, J., Stephdut, Mazloff, M., Fox-Kemper, B., Antnguyen13, Doddridge, E., Fenty, I., Bates, M., AndrewEichmann-NOAA, Smith, T., Martin, T., Lauderdale, J., Abernathey, R., Samarkhatiwala, Hongandyan, Deremble, B., Dngoldberg, Bourgault, P., and Dussin, R.: MITgcm/MITgcm: checkpoint67z, https://doi.org/10.5281/ZENODO.4968496, 2021.

Campin, J.-M., Heimbach, P., Losch, M., Forget, G., edhill3, Adcroft, A., amolod, Menemenlis, D., dfer22, Jahn, O., Hill, C., Scott, J., dngoldberg, stephdut, Mazloff, M., Fox-Kemper, B., antnguyen13, Doddridge, E., Fenty, I., Bates, M., Wang, O., Smith, T., AndrewEichmann-NOAA, mitllheisey, Lauderdale, J., Martin, T., Abernathey, R., samarkhatiwala, hongandyan, and averdy: dringeis/MITgcm: Mohr-Coulomb rheologies, https://doi.org/10.5281/zenodo.19361862, 2026.

Chatta, S., Khouider, B., and Kesri, M.: Linear well posedness of regularized equations of sea-ice dynamics, Journal of Mathematical Physics, 64, 051 504, https://doi.org/10.1063/5.0152991, 2023.

Coulomb, C.: Test on the applications of the rules of maxima and minima to some problems of statics related to architecture, Mem Math Phys, 7, 343–382, 1773.

Damsgaard, A., Adcroft, A., and Sergienko, O.: Application of Discrete Element Methods to Approximate Sea Ice Dynamics, Journal of Advances in Modeling Earth Systems, 10, 2228–2244, https://doi.org/10.1029/2018MS001299, _eprint: https://onlinelibrary.wiley.com/doi/pdf/10.1029/2018MS001299, 2018.

Dansereau, V., Weiss, J., Saramito, P., and Lattes, P.: A Maxwell elasto-brittle rheology for sea ice modelling, The Cryosphere, 10, 1339–1359, https://doi.org/10.5194/tc-10-1339-2016, 2016.

Dansereau, V., Démery, V., Berthier, E., Weiss, J., and Ponson, L.: Collective Damage Growth Controls Fault Orientation in Quasibrittle Compressive Failure, Physical Review Letters, 122, 085 501, https://doi.org/10.1103/PhysRevLett.122.085501, 2019.

de Borst, R., Sabet, S. A., and Hageman, T.: Non-associated Cosserat plasticity, International Journal of Mechanical Sciences, 230, 107 535, https://doi.org/10.1016/j.ijmecsci.2022.107535, 2022.

Flato, G. M. and Hibler, W. D.: Modeling Pack Ice as a Cavitating Fluid, Journal of Physical Oceanography, 22, 626–651, https://doi.org/10.1175/1520-0485(1992)022<0626:MPIAAC>2.0.CO;2, 1992.

Handin, J.: On the Coulomb-Mohr failure criterion, Journal of Geophysical Research (1896-1977), 74, 5343–5348, https://doi.org/https://doi.org/10.1029/JB074i022p05343, _eprint: https://agupubs.onlinelibrary.wiley.com/doi/pdf/10.1029/JB074i022p05343, 1969.

Herman, A.: Discrete-Element bonded-particle Sea Ice model DESIgn, version 1.3a - model description and implementation, Geoscientific Model Development, 9, https://doi.org/10.5194/gmd-9-1219-2016, 2016.

Hibler, W. D.: A Dynamic Thermodynamic Sea Ice Model, Journal of Physical Oceanography, 9, 815–846, https://doi.org/10.1175/1520-0485(1979)009<0815:ADTSIM>2.0.CO;2, 1979.

Hibler, W. D. and Schulson, E. M.: On modeling the anisotropic failure and flow of flawed sea ice, Journal of Geophysical Research: Oceans, 105, 17 105–17 120, https://doi.org/10.1029/2000JC900045, 2000.

Hutchings, J. K., Heil, P., and Hibler, W. D.: Modeling Linear Kinematic Features in Sea Ice, Monthly Weather Review, 133, 3481–3497, https://doi.org/10.1175/MWR3045.1, 2005.

Hutter, N., Bouchat, A., Dupont, F., Dukhovskoy, D., Koldunov, N., Lee, Y. J., Lemieux, J.-F., Lique, C., Losch, M., Maslowski, W., Myers, P. G., Ólason, E., Rampal, P., Rasmussen, T., Talandier, C., Tremblay, B., and Wang, Q.: Sea Ice Rheology Experiment (SIREx): 2. Evaluating Linear Kinematic Features in High-Resolution Sea Ice Simulations, Journal of Geophysical Research: Oceans, 127, e2021JC017 666, https://doi.org/10.1029/2021JC017666, _eprint: https://onlinelibrary.wiley.com/doi/pdf/10.1029/2021JC017666, 2022.

Ip, C. F., Hibler, W. D., and Flato, G. M.: On the effect of rheology on seasonal sea-ice simulations, Annals of Glaciology, 15, 17–25, 1991.

Kaus, B. J. P.: Factors that control the angle of shear bands in geodynamic numerical models of brittle deformation, Tectonophysics, 484, 36–47, https://doi.org/10.1016/j.tecto.2009.08.042, 2010.

Kimmritz, M., Danilov, S., and Losch, M.: The adaptive EVP method for solving the sea ice momentum equation, Ocean Modelling, 101, 59–67, https://doi.org/10.1016/j.ocemod.2016.03.004, 2016.

König Beatty, C. and Holland, D. M.: Modeling Landfast Sea Ice by Adding Tensile Strength, Journal of Physical Oceanography, 40, 185–198, https://doi.org/10.1175/2009JPO4105.1, 2010.

Lemiale, V., Mühlhaus, H. B., Moresi, L., and Stafford, J.: Shear banding analysis of plastic models formulated for incompressible viscous flows, Physics of the Earth and Planetary Interiors, 171, 177–186, https://doi.org/10.1016/j.pepi.2008.07.038, 2008.

Lemieux, J.-F. and Dupont, F.: On the calculation of normalized viscous–plastic sea ice stresses, Geoscientific Model Development, 13, 1763–1769, https://doi.org/10.5194/gmd-13-1763-2020, publisher: Copernicus GmbH, 2020.

Lemieux, J.-F. and Tremblay, B.: Numerical convergence of viscous-plastic sea ice models, Journal of Geophysical Research: Oceans, 114, https://doi.org/10.1029/2008JC005017, 2009.

Lemieux, J.-F., Tremblay, B., Sedláček, J., Tupper, P., Thomas, S., Huard, D., and Auclair, J.-P.: Improving the numerical convergence of viscous-plastic sea ice models with the Jacobian-free Newton–Krylov method, Journal of Computational Physics, 229, 2840–2852, https://doi.org/10.1016/j.jcp.2009.12.011, 2010.

© Author(s) 2026. CC BY 4.0 License.

Lemieux, J.-F., Plante, M., Hutter, N., Ringeisen, D., Tremblay, B., Roy, F., and Blain, P.: Impact of non-normal flow rule on linear kinematic features in pan-Arctic ice-ocean simulations, The Cryosphere, 19, 5639–5654, https://doi.org/10.5194/tc-19-5639-2025, publisher: Copernicus GmbH, 2025.

Lipscomb, W. H.: Remapping the thickness distribution in sea ice models, Journal of Geophysical Research: Oceans, 106, 13 989–14 000, https://doi.org/10.1029/2000JC000518, _eprint: https://onlinelibrary.wiley.com/doi/pdf/10.1029/2000JC000518, 2001.

Losch, M., Menemenlis, D., Campin, J.-M., Heimbach, P., and Hill, C.: On the formulation of sea-ice models. Part 1: Effects of different solver implementations and parameterizations, Ocean Modelling, 33, 129–144, https://doi.org/10.1016/j.ocemod.2009.12.008, 2010.

Marshall, J., Adcroft, A., Hill, C., Perelman, L., and Heisey, C.: A finite-volume, incompressible Navier Stokes model for studies of the ocean on parallel computers, Journal of Geophysical Research: Oceans, 102, 5753–5766, https://doi.org/10.1029/96JC02775, 1997.

Mohr, O.: Ueber die Darstellung des Spannungszustandes eines Korperelements, Civilengenieur, 28, pp.113–56., 1882.

Plante, M. and Tremblay, L. B.: A generalized stress correction scheme for the Maxwell elasto-brittle rheology: impact on the fracture angles and deformations, The Cryosphere, 15, 5623–5638, https://doi.org/10.5194/tc-15-5623-2021, publisher: Copernicus GmbH, 2021.

Ringeisen, D., Losch, M., Tremblay, L. B., and Hutter, N.: Simulating intersection angles between conjugate faults in sea ice with different viscous–plastic rheologies, The Cryosphere, 13, 1167–1186, https://doi.org/https://doi.org/10.5194/tc-13-1167-2019, 2019.

Ringeisen, D., Tremblay, L. B., and Losch, M.: Non-normal flow rules affect fracture angles in sea ice viscous–plastic rheologies, The Cryosphere, 15, 2873–2888, https://doi.org/10.5194/tc-15-2873-2021, publisher: Copernicus GmbH, 2021.

Ringeisen, D., Hutter, N., and von Albedyll, L.: Deformation lines in Arctic sea ice: intersection angle distribution and mechanical properties, The Cryosphere, 17, 4047–4061, https://doi.org/10.5194/tc-17-4047-2023, publisher: Copernicus GmbH, 2023a.

Ringeisen, D., Losch, M., and Tremblay, L. B.: Teardrop and Parabolic Lens Yield Curves for Viscous-Plastic Sea Ice Models: New Constitutive Equations and Failure Angles, Journal of Advances in Modeling Earth Systems, 15, e2023MS003 613, https://doi.org/10.1029/2023MS003613, _eprint: https://onlinelibrary.wiley.com/doi/pdf/10.1029/2023MS003613, 2023b.

Roscoe, K. H.: The Influence of Strains in Soil Mechanics, Géotechnique, 20, 129–170, https://doi.org/10.1680/geot.1970.20.2.129, 1970.

Rothrock, D. A.: The Mechanical Behavior of Pack ICE, Annual Review of Earth and Planetary Sciences, 3, 317–342, https://doi.org/10.1146/annurev.ea.03.050175.001533, 1975.

Schulson, E. M.: Compressive shear faults within arctic sea ice: Fracture on scales large and small, Journal of Geophysical Research: Oceans, 109, C07 016, https://doi.org/10.1029/2003JC002108, 2004.

Schulson, E. M., Fortt, A. L., Iliescu, D., and Renshaw, C. E.: Failure envelope of first-year Arctic sea ice: The role of friction in compressive fracture, Journal of Geophysical Research: Oceans, https://doi.org/10.1029/2005JC003235, publisher: John Wiley & Sons, Ltd, 2006.

Stern, H. L., Rothrock, D. A., and Kwok, R.: Open water production in Arctic sea ice: Satellite measurements and model parameterizations, Journal of Geophysical Research: Oceans, 100, 20 601–20 612, https://doi.org/10.1029/95JC02306, publisher: John Wiley & Sons, Ltd, 1995.

Tremblay, L.-B. and Mysak, L. A.: Modeling Sea Ice as a Granular Material, Including the Dilatancy Effect, Journal of Physical Oceanography, 27, 2342–2360, https://doi.org/10.1175/1520-0485(1997)027<2342:MSIAAG>2.0.CO;2, 1997.

Vardoulakis, I.: Shear-banding and liquefaction in granular materials on the basis of a Cosserat continuum theory, Ingenieur-Archiv, 59, 106–113, https://doi.org/10.1007/BF00538364, 1989.

Vermeer, P. A.: The orientation of shear bands in biaxial tests, Géotechnique, https://doi.org/10.1680/geot.1990.40.2.223, 1990.

Verruijt, A.: An Introduction to Soil Mechanics, Theory and Applications of Transport in Porous Media, Springer International Publishing, ISBN 978-3-319-61184-6, https://doi.org/10.1007/978-3-319-61185-3, 2018.

© Author(s) 2026. CC BY 4.0 License.

Wang, K. and Wang, C.: Modeling linear kinematic features in pack ice, Journal of Geophysical Research: Oceans, 114, https://doi.org/10.1029/2008JC005217, 2009.

Weiss, J. and Schulson, E. M.: Coulombic faulting from the grain scale to the geophysical scale: lessons from ice, Journal of Physics D: Applied Physics, 42, 214 017, https://doi.org/10.1088/0022-3727/42/21/214017, 2009.

Weiss, J., Schulson, E. M., and Stern, H. L.: Sea ice rheology from in-situ, satellite and laboratory observations: Fracture and friction, Earth and Planetary Science Letters, 255, 1–8, https://doi.org/10.1016/j.epsl.2006.11.033, 2007.

Zhang, J. and Hibler, W. D.: On an efficient numerical method for modeling sea ice dynamics, Journal of Geophysical Research: Oceans, 102, 8691–8702, https://doi.org/10.1029/96JC03744, 1997.

Zhang, J. and Rothrock, D. A.: Effect of sea ice rheology in numerical investigations of climate, Journal of Geophysical Research: Oceans, 110, C08 014, https://doi.org/10.1029/2004JC002599, 2005.

Åström, J., Haapala, J., and Polojärvi, A.: A large-scale high-resolution numerical model for sea-ice fragmentation dynamics, The Cryosphere Discussions, pp. 1–16, https://doi.org/10.5194/tc-2023-97, publisher: Copernicus GmbH, 2023.